Translational Science

Cancer Research

New Mechanisms of Resistance to MEK Inhibitors in Melanoma Revealed by Intravital Imaging

Hailey E. Brighton[1,2], Steven P. Angus[3], Tao Bo[1], Jose Roques[1], Alicia C. Tagliatela[1,2], David B. Darr[1], Kubra Karagoz[4], Noah Sciaky[3], Michael L. Gatza[4], Norman E. Sharpless[1,5,6], Gary L. Johnson[1,3], and James E. Bear[1,2,3]

Abstract

Targeted therapeutics that are initially effective in cancer patients nearly invariably engender resistance at some stage, an inherent challenge in the use of any molecular-targeted drug in cancer settings. In this study, we evaluated resistance mechanisms arising in metastatic melanoma to MAPK pathway kinase inhibitors as a strategy to identify candidate strategies to limit risks of resistance. To investigate longitudinal responses, we developed an intravital serial imaging approach that can directly visualize drug response in an inducible RAF-driven, autochthonous murine model of melanoma incorporating a fluorescent reporter allele (tdTomatoLSL). Using this system, we visualized formation and progression of tumors *in situ*, starting from the single-cell level longitudinally over time. Reliable reporting of the status of primary murine tumors treated with the selective MEK1/2 inhibitor (MEKi) trametinib illustrated a time-course of initial drug response and persistence, followed by the development of drug resistance. We found that tumor cells adjacent to bundled collagen had a preferential persistence in response to MEKi. Unbiased transcriptional and kinome reprogramming analyses from selected treatment time points suggested increased c-Kit and PI3K/AKT pathway activation in resistant tumors, along with enhanced expression of epithelial genes and epithelial-mesenchymal transition downregulation signatures with development of MEKi resistance. Similar trends were observed following simultaneous treatment with BRAF and MEK inhibitors aligned to standard-of-care combination therapy, suggesting these reprogramming events were not specific to MEKi alone. Overall, our results illuminate the integration of tumor–stroma dynamics with tissue plasticity in melanoma progression and provide new insights into the basis for drug response, persistence, and resistance.

Significance: A longitudinal study tracks the course of MEKi treatment in an autochthonous imageable murine model of melanoma from initial response to therapeutic resistance, offering new insights into the basis for drug response, persistence, and resistance. *Cancer Res; 78(2); 542–57. ©2017 AACR.*

Introduction

Activating mutations in the MAPK pathway drive malignant transformation in melanoma, with BRAF(V600E) being the most common driver in patient settings (1–3). Clinical use of selective MEK and BRAF inhibitors (MEKi and BRAFi) have extended overall survival in patients with BRAF-mutant melanoma (4–6). Although initially effective, resistance to these targeted therapies eventually develops, even in patients given combined BRAFi/MEKi therapy (5, 7, 8). A number of mechanisms have been suggested for how melanoma can become refractory to therapy, including increased PI3K and AKT pathway activity, enhanced expression of receptor tyrosine kinases (e.g., c-KIT, FGFR, and EGFR), and compensation for BRAF activity through NRAS mutation or CRAF or ARAF upregulation (9–11). Despite this work, there exists a substantial need for relevant preclinical models to analyze therapeutic response *in vivo* in order to make better prognostic predictions and to inform treatment strategies (12).

A complex variety of genomic, epigenetic, and extracellular factors all affect how melanoma responds to and resists therapeutic intervention. Evidence of "phenotype switching" at the molecular level has also been identified as a relevant mechanism for how tumors become resistant to targeted therapy (13–15). Via this mechanism, tumor cells may adapt a stem-like phenotype, and a "switch" from epithelial to mesenchymal phenotype has been documented in a variety of tumors in response to drug, which is thought to promote malignancy and therapy resistance (16).

Melanoma cell heterogeneity, which is driven by both switches in molecular expression and changes in the extracellular microenviroment, also influences therapeutic resistance (17, 18). Exactly how the extracellular matrix (ECM) affects tumor response to drug remains unclear. It is known that collagen in tumors is commonly cross-linked in linear bundles, which can stiffen the microenvironment and elicit downstream signaling events that promote tumorigenesis (19, 20). Improving our understanding of how therapeutics influence the ECM within the tumor microenvironment is critical, as collagen deposition and reorganization may promote melanoma cell invasion, malignancy, and resistance through multiple mechanisms (21, 22). Furthermore,

[1]UNC Lineberger Comprehensive Cancer Center, University of North Carolina at Chapel Hill, Chapel Hill, North Carolina. [2]Department of Cell Biology and Physiology, University of North Carolina at Chapel Hill, Chapel Hill, North Carolina. [3]Department of Pharmacology, University of North Carolina at Chapel Hill, Chapel Hill, North Carolina. [4]Department of Radiation Oncology, Rutgers Cancer Institute of New Jersey, New Brunswick, New Jersey. [5]Department of Medicine, University of North Carolina at Chapel Hill, Chapel Hill, North Carolina. [6]Department of Genetics, University of North Carolina at Chapel Hill, Chapel Hill, North Carolina.

Note: Supplementary data for this article are available at Cancer Research Online (http://cancerres.aacrjournals.org/).

H.E. Brighton and S.P. Angus contributed equally to this article.

Corresponding Author: James E. Bear, Lineberger Comprehensive Cancer Center, University of North Carolina at Chapel Hill, Room 21-223, CB 7295, Chapel Hill, NC 27599. Phone: 919-966-5471; Fax: 919-966-3015; E-mail: jbear@email.unc.edu

doi: 10.1158/0008-5472.CAN-17-1653

AACR

intratumoral regions with high stromal cell concentrations have been shown to promote tumor cell persistence against BRAF inhibitor (23). Modeling ECM behavior in tumor development and drug response through proper *in vivo* strategies can help uncover new therapeutic approaches and targets (24).

To address the challenges of modeling response and resistance to targeted therapies, we have extended an existing *Tyr::CreER; BRAF*^{CA};*PTEN*$^{lox/lox}$ (PBT) genetically engineered murine (GEM) model of melanoma by crossing in a Lox-Stop-Lox tdTomato fluorescent reporter allele (tdTomato^{LSL}; refs. 25, 26). The incorporation of this allele enables direct tracking of endogenous melanoma development and therapeutic response over time through noninvasive intravital imaging. With a highly localized application method of 4-hydroxytamoxifen (4-HT) on the mouse ear, we have achieved precise spatiotemporal control of melanoma initiation. Using this approach, we directly visualized tumor and collagen reorganization throughout development and response to single-agent trametinib (a highly potent, allosteric MEKi; ref. 27) and trametinib/dabrafenib combination MEKi/BRAFi therapy. We also identified changes in molecular behavior through transcriptome and kinome reprogramming analysis at early and late stages on therapy, providing a comprehensive view of melanoma response to MAPKi.

Materials and Methods

Local 4-HT application method

All animal studies have been conducted in accordance with guidance from the Institutional Animal Care and Use Committee at University of North Carolina-Chapel Hill (Chapel Hill, NC). To achieve spatially controlled melanocyte recombination by local topical application, we applied 1 μL of a 20 mmol/L concentration of 4-HT solution in DMSO, 100% ethanol, and orange-6 dye to allow precise visualization of the region exposed to 4-HT, in which CreER is activated (Sigma-Aldrich), to the middle of the ear while the mouse was anesthetized. After 8 to 10 minutes, the area was vigorously washed with 70% EtOH to prevent transfer of tamoxifen to other areas and to ensure a single, controlled primary lesion (Fig. 1B). Using this method, we consistently induced local melanoma growth exclusively in the applied region in a reproducible fashion.

Intravital two-photon microscopy

Tumor-bearing animals with tumors between 10 and 30 mm^3 were imaged as previously described (28). Animals were anesthetized with 1% to 2% isoflurane on a heating pad equipped with temperature feedback, and tumors were imaged before and during the course of drug treatment studies. All imaging was performed on an Olympus FV1000MPE with an Insight DeepSee IR laser (Spectra-Physics) and an upright BX-61WI microscope, using a 25×, 1.05 NA (2 mm TRAMETINIB.D.) water immersion objective with optical imaging gel with the same refractive index as water to capture images. Laser was tuned to 1,050 nm to excite tdTomato fluorescence. A custom aluminum ear clamp, with (i) a bottom platform on which the ear rests and (ii) an upper piece equipped with a pair of thumbscrews to secure the ear underneath a coverslip, facilitated transfer of heat to the ear from an underlying heating plate/pad during imaging. Laser power (4%), software, and microscope settings (RXD2 and RXD4 channel PMT voltages at 850 and 500, respectively) were consistent for all acquired images. Two channel non-descan detectors were used for image collection, and data were gathered with the Olympus Fluoview software.

Macroscopic imaging of tdTomato positive tumors

Macroscopic imaging was performed on an Olympus MVX10 macroscope system, and images were collected using Metamorph software and a color camera at ×0.8 or ×1 magnification. Fluorescent images were acquired using a mercury lamp and filter wheel for red fluorescence. Mice were anesthetized with 1% to 2% isoflurane and placed on a heating pad during imaging. Ears were flattened and stabilized to 5-mL tubes with double-sided tape to enable full macroscopic view of each tumor.

Histology of tumor progression and tumor response to trametinib

Ears and lymph nodes were excised and fixed in 4% paraformaldehyde at 4°C for 24 hours. Tissues were then cryoprotected with fresh 30% sucrose at 4°C for 24 hours. Ears and lymph nodes were then frozen in VWR Clear Frozen Section Compound (VWR 95057) using an ethanol/dry ice bath and were stored at −80°C before sectioning. Sectioning and hematoxylin and eosin staining were performed by the Cell Biology & Physiology Histology Core at University of North Carolina-Chapel Hill.

Drug treatments and further mouse protocols

A total of 0.3 milligrams per kilogram (mpk) trametinib (GSK212) powdered compound or, for combination studies, 0.3 mpk trametinib + 18 mpk dabrafenib powdered compound mixture was added to a base mixture, which was added to normal food/chow mixture before being pelleted by Research Diets, Inc. Prepared chow was fed to mice, which were harvested at 1 and 12 weeks on drug treatment. Tumor measurements were performed with a digital caliper every week during the course of each experiment, and measurements for length, width, and height were recorded (in mm). Tumor size was indicated by tumor depth. Mice were carefully monitored in accordance with our protocol.

Fluorescence intensity analysis

Maximum intensity projections were made from z-stacks with 4-μm intervals, taken with FV1000MPE two-photon, (roughly 20–40 slices per image, depending on tumor depth). Average intensity was measured using Metamorph software analysis, and the intensity for each image was normalized by subtracting the value for background average fluorescence. Measurements were averaged for each time point, post-4-OHT application, plotted in Excel, and graphed in Prism. Each image was acquired with 4% laser power to maintain consistency.

Multiplexed inhibitor bead chromatography and mass spectrometry

Snap-frozen tumors were crushed by mortar and pestle in ice-cold multiplexed inhibitor bead (MIB) lysis buffer (50 mmol/L HEPES, 150 mmol/L NaCl, 0.5% Triton X-100, 1 mmol/L EDTA, 1 mmol/L EGTA, pH 7.5) supplemented with complete protease inhibitor cocktail (Roche) and 1% phosphatase inhibitor cocktails 2 and 3 (Sigma). Extracts were sonicated 3 × 10 seconds, clarified by centrifugation, and syringe-filtered (0.22 μm) prior to Bradford assay quantitation of concentration. Equal amounts of total protein (0.3 mg) were gravity-flowed over MIB columns in high salt MIB lysis (1 mol/L NaCl). The MIB columns consisted of

175-μL mixture of six type I kinase inhibitors (CTx-0294885, VI-16832, PP58, Purvalanol B, UNC-21474, and UNC-8088A) custom-synthesized with hydrocarbon linkers and covalently linked to ECH-Sepharose (or EAH-Sepharose for Purvalanol B) beads as previously described (29). Columns were washed with 5 mL of high salt (1 mol/L NaCl), 5 mL of low salt (150 mmol/L NaCl) MIB lysis buffer, and 0.5 mL low-salt lysis buffer with 0.1% SDS. Bound protein was eluted twice with 0.5% SDS, 1% β-mercaptoethanol, 100 mmol/L Tris-HCl, pH 6.8 for 15 minutes at 100°C. Eluate was treated with DTT (5 mmol/L) for 25 minutes at 60°C and 20 mmol/L iodoacetamide for 30 minutes in the dark. Following spin concentration using Amicon Ultra-4 (10k cut-off) to approximately 100 μL, samples were precipitated by methanol/chloroform, dried in a speed-vac and resuspended in 50 mmol/L HEPES (pH 8.0). Tryptic digests were performed overnight at 37°C, extracted four times with 1 mL ethyl acetate to remove detergent, dried in a speed-vac, and peptides further cleaned using C-18 spin columns according to manufacturer's protocol (Pierce).

RNA isolation, RNA-seq library preparation, RNA-seq, and analysis

A center section of each snap-frozen tumor was excised with a clean razor blade and RNA isolated using the RNeasy Plus Mini Kit (Qiagen) according to manufacturer's protocol with the optional DNase I treatment (Qiagen) for 15 minutes. Four hundred nanograms of total RNA was used as input for RNA-seq library construction with a Kapa Stranded mRNA Kit according to the manufacturer's protocol. TruSeq adapter sequences were used for indexing. Library amplification was as described with 12 PCR cycles. Equimolar amounts of each library were run as multiplexed1.65 pM pools, single-indexed, on a NextSeq 500–75 cycle, high output V2 Kit. QC-passed reads were aligned to the mouse reference genome (mm9) using MapSplice (30). The alignment profile was determined by Picard Tools v1.64. Aligned reads were sorted and indexed using SAMtools and translated to transcriptome coordinates and filtered for indels, large inserts, and zero mapping quality using UBU v1.0. Transcript abundance estimates for each sample were performed using an expectation–maximization algorithm, RSEM (31). Expected read counts for genes were used as input for DESeq2 to identify differentially expressed genes (32). Differentially expressed gene sets ($P_{adj} < 0.1$) were used as input for Enrichr (33, 34) to identify pathway enrichments. Heat maps of log_2-transformed RSEM normalized expression values were generated using GENE-E software (Broad Institute). Normalized RSEM mouse gene values were converted to unique human gene IDs by shared Homologene ID. Pathway signatures were determined as previously described (35, 36).

Cell lines and drug treatments

The human melanoma cell lines used, A375, SK-MEL-190, WM266-4, SK-MEL-100, SK-MEL-5, and Mel537, have been extensively characterized (37). Cells are routinely tested for mycoplasma contamination by DAPI staining and passaged no more than 1 month prior to experiments. Cells were cultured in DMEM (A375, WM266-4) or RPMI (SK-MEL-190, SK-MEL-100, SK-MEL-5, and Mel537) supplemented with 10% FBS and 1% penicillin–streptomycin. Dabrafenib and trametinib were purchased from Selleck and dissolved in DMSO. Cultures were treated with DMSO as control or with 100 nmol/L dabrafenib and 10 nmol/L trametinib in combination for 48 trametinib.

Western blotting

Snap-frozen mouse tumors or human melanoma cell lines were extracted in MIB lysis buffer (150 mmol/L NaCl) as above and filtered lysates were boiled in 1× SDS sample buffer for 10 minutes at 100°C. Equal amounts of lysate were separated by SDS-PAGE, transferred to nitrocellulose membrane, blocked with 5% milk in TBS, and subjected to immunoblotting with the following primary antibodies: PDGFRβ, DDR1, phospho-ERK1/2 (218/222), MEK1/2, phospho-MEK1/2, SOX2, and E-cadherin, from Cell Signaling Technology; pan-Cytokeratin, BRAF, c-Kit, SOX10, and ERK2 from Santa Cruz Biotechnology; RFP (to detect tdTomato) from Rockland; SOX21 from Protein-Tech. Secondary antibodies used were goat anti-rabbit-HRP or goat anti-mouse-HRP from Pierce Biotechnology. SuperSignal West Pico Chemiluminescent Substrate (Thermo Scientific) was used and images were collected on a Bio-Rad ChemiDoc.

Liquid chromatography, mass spectrometry, and analysis

Peptides were resuspended in 2% ACN and 0.1% formic acid. Forty percent of the final peptide suspension was injected onto a Thermo Easy-Spray 75 μm × 25 cm C-18 column and separated on a 180 minutes gradient (5–40% ACN) using an Easy nLC-1000. The Thermo Q Exactive mass spectrometry (MS) ESI parameters were as follows: 3e6 AGC MS1, 80 milliseconds MS1 max inject time, 1e5 AGC MS2, 100 milliseconds MS2 max inject time, 20 loop count, 1.8 m/z isolation window, 45 seconds dynamic exclusion. Raw files were processed for label-free quantification (LFQ) by MaxQuant LFQ using the Uniprot/Swiss-Prot mouse database and default parameters were used with the following exceptions—only unique peptides were used, matching between runs was utilized, and phospho-STY peptides were included. Normalized LFQ intensities were log_2-transformed and hierarchical clustering (1−Pearson correlation) performed using GENE-E or imported into Perseus software. In Perseus, LFQ intensities were log_2-transformed, missing values were imputed from the matrix if at least three valid values were present in at least one treatment group, and two-sample t tests were performed with permutation-based false discovery rate (FDR; 5% cutoff).

Analysis of SOX transcription factor expression

Normalized, log_2-transformed expression data (GSE99898) from patient samples pretreatment, early during treatment (EDT), or at progression on dabrafenib, vemurafenib, or dabrafenib and trametinib was retrieved from the Gene Expression Omnibus (GEO; ref. 38). Log_2 difference in gene expression for the SOX transcription factors was determined relative to pretreatment for each matched patient sample and hierarchical clustering was performed using Morpheus software (Broad Institute).

Results

Specific 4-HT application method enables spatiotemporal control of tumor growth

Although inducible GEM models of cancer have enhanced our understanding of tumor biology and therapeutic response, there exists a significant need to improve these models for translational research (39). The ability to control endogenous tumor initiation in time and space is a critical experimental variable that needs to be improved to better model melanoma as it occurs in patients. We developed a precise induction

method, where 1 μL of 20 mmol/L 4-HT was applied to the middle of the mouse ear for 8–10 minutes then carefully removed and the area washed. We chose to induce melanoma on the ear because the skin of the mouse ear contains a population of intrafollicular melanocytes that more closely mirrors human skin, and the ear provides an ideal surface for stable intravital imaging (39, 40). Our imaging strategy incorporated a tdTomato fluorescent reporter allele (tdTomato^{LSL}) in the existing tamoxifen-inducible PBT melanoma GEM model (Fig. 1A; refs. 25, 26). This method of 4-HT application yielded robust local tumor formation on mouse ears in a reproducible fashion; tumors forming with 100% penetrance (Fig. 1B; Supplementary Fig. S1). In addition, precise spatiotemporal control of melanoma induction in this GEM model extended animal lifespan (normally limited by multiple primary tumors), which enabled long-term longitudinal *in vivo* studies of melanoma development and, later, drug response.

Visualizing the process of endogenous tumor progression from early stages has been a relative "black box" in the field, as most existing models cannot be used to track tumor cell behavior over time at cellular resolution. We used two previously described intravital imaging methods to interrogate tdTomato$^+$ PBT melanoma behavior both at the macroscopic (mm) and microscopic (μm) scale using a stereomicroscope and a multiphoton microscope, respectively (Supplementary Fig. S1A and S1B; ref. 28). Using anesthetized animals, we positioned them on a heating pad and stabilized the ear with a custom designed ear clamp during imaging. With multiphoton imaging, we were able to quantify the original number of recombined melanocytes postinduction. Less than 2 days after 4-HT treatment, we identified individual recombined endogenous melanocytes within the dermis (Supplementary Fig. S1). At this stage, we counted the tdTomato$^+$ melanoma cells in a 1.2-mm^2 region (140 cells/mm^2) and approximated the total number of recombined cells that are initially induced by extrapolating from the average area of the 4-HT droplet (2.77 mm^2, $n = 20$; Supplementary Fig. S1C and S1D). We identified different populations of recombined tdTomato$^+$ cells, including both intra- and interfollicular melanocytes within the dermis, and calculated less than 400 melanocytes initially recombined in this system with 20 mmol/L 4-HT to yield reproducible tumor formation (Supplementary Fig. S1E and S1F).

Next, we imaged PBT melanoma progression from early stages serially over time to characterize melanoma development in this model. Tracking tumors each week post-4-HT application via transmitted light and fluorescence imaging revealed stages of tumor growth that were reproducible from tumor to tumor at different time points (Fig. 1C). At the macroscopic level, melanoma initially spread radially, forming a palpable tumor mass within 6–8 weeks postapplication of 4-HT, and we observed relatively homogeneous tdTomato distribution throughout tumor growth, even in separate cohorts (Fig. 1D, data not shown). Melanoma growth, measured by tumor depth, was exponential, and there was no evidence of tumor development in other regions on the animal (Fig. 1E; Supplementary Fig. S1G). Furthermore, breeding out the Pten$^{lox/lox}$ and BRAF^{CA} alleles yielded a control Tyr::CreER; tdTomato^{LSL} mouse line for comparison with nontumorigenic fluorescent melanocytes, which were dendritic and did not proliferate to form melanoma (Supplementary Fig. S2A).

Longitudinal intravital imaging reveals distinct phases of melanoma development

Multiphoton imaging provided a platform to simultaneously visualize tdTomato$^+$ melanoma cells and second harmonic generation (SHG), which enabled detection of the bundled collagen fiber network in the tumor microenvironment (42). Using the SHG as a guide, we visualized the tumor cells throughout the dermis (depth range of 30–200 μm), between the epidermis and the cartilage layer in the middle of the mouse ear. In addition, we identified known structures such as hair follicles, which are evident by their circular structure and a center devoid of fluorescence.

By tracking the tdTomato$^+$ melanoma cells in concert with the SHG, we followed melanoma development from early stages with cellular resolution, and we identified distinct phases of growth (Fig. 2A; Supplementary Fig. S2B). During the "proliferation phase," the first few weeks post-4-HT application, we identified clonal populations of melanoma cells arising directly in the dermis. These regions of concentrated tdTomato$^+$ cells expanded over time to become densely packed pretumorous lesions. From there, tdTomato$^+$ cells spread radially throughout the dermis, during the "pre" (2–4 weeks) and "early tumor" (4–6 weeks) phases, where the dermis became dense with tdTomato$^+$ melanoma cells. During this phase, SHG signal was significantly reduced, suggesting degradation of bundled collagen and the ECM. Here, we also clearly identified the tumor boundary in the ear at the cell level (Supplementary Fig. S2C, white line). Finally, the "late tumor phase" (7+ weeks), corresponded with the vertical growth phase in patient settings, as melanomas rose above the original flat surface of the ear (Figs. 1D and 2A). Fluorescence intensity analysis at these different stages of tumor development further recapitulated our ability to model clinical tumor growth, as tdTomato increased and SHG signal decreased over time (Fig. 2B and C).

To compare our *ad hoc* intravital staging series to more traditional approaches, we used classic histology techniques to characterize tumor progression in this model via hematoxylin and eosin staining. Consistent with our intravital imaging, tissue thickness increased over time, and infiltration of stromal cell populations and increased tumor cell concentrations were evident (Fig. 2D). Masson's trichrome (MT) staining further demonstrated the degradation of collagen post-4-HT application (Fig. 2E). Because the tdTomato signal was conserved after tissue processing for histology, we also performed fluorescence microscopy of histologic sections to visualize tumor development at different phases (Fig. 2F; Supplementary Fig. S2D). With this technique, in the "proliferation phase," we saw a small population of tdTomato$^+$ cells on the dorsal part of the mouse ear where 4-HT was applied. In the early and late tumor phases, however, we identified vertical growth in both ventral and dorsal regions of the ear, and at the "late tumor phase," we identified melanoma cell invasion through the cartilage layer in the middle of the ear (Supplementary Fig. S2D).

Through defining distinct phases of melanoma development *in situ* from the initial time point, our system provides a mechanism to visualize tumor cell behavior in a variety of different investigative platforms. We envision that this system can be used to interrogate distinct and relevant hallmarks of early tumor behavior *in vivo*, such as tumor angiogenesis, tumor–stroma interactions, and invasion prior to vertical growth (43). However, because our main objective was to create a model of long-term

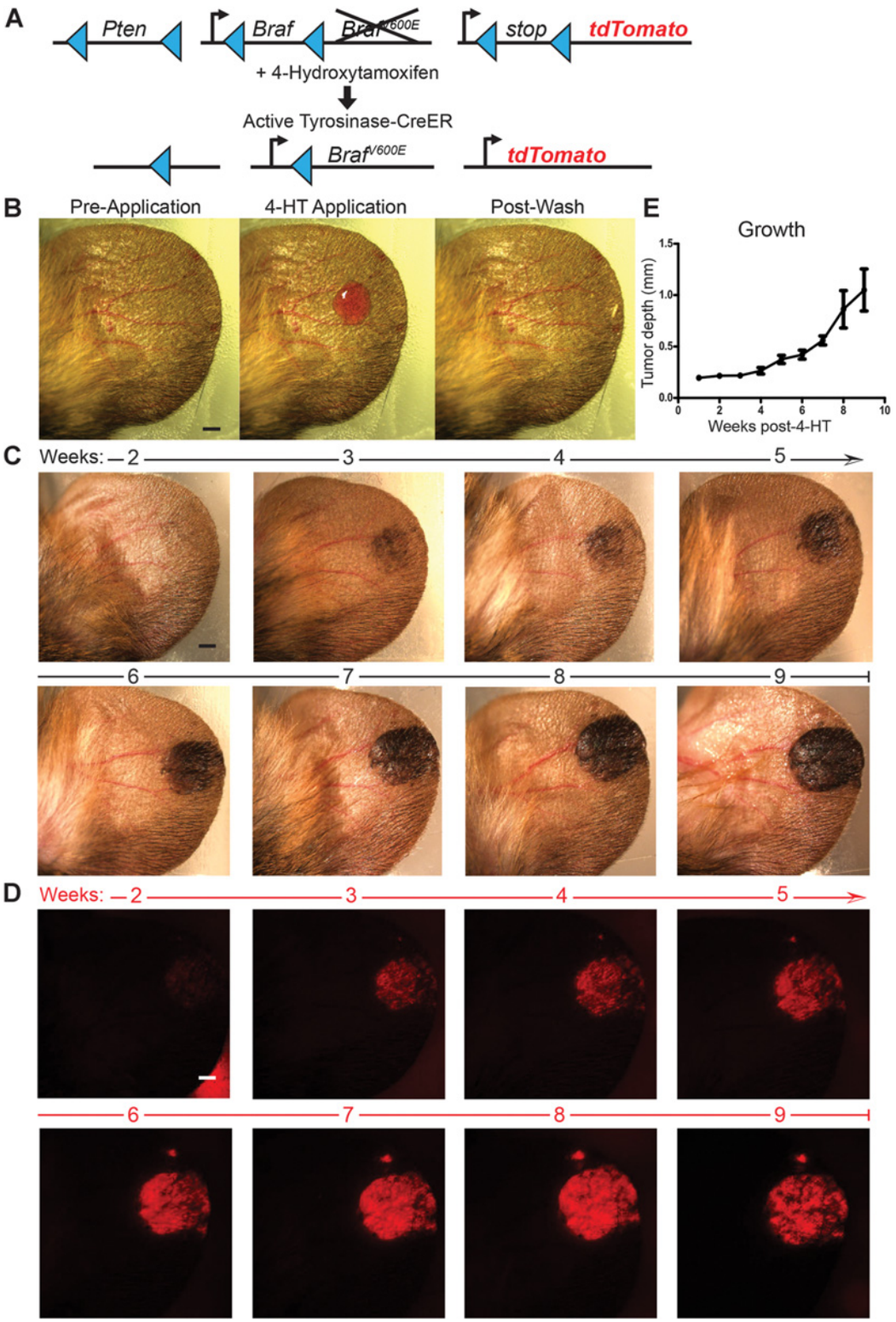

Figure 1.

Genetic incorporation of tdTomato enables visualization of melanoma initiation and growth with specific 4-HT application method. **A,** Diagram of PBT (*Tyr::CreER; BRAF*^{CA}*;PTEN*$^{lox/lox}$*;tdTomato*^{LSL}) melanoma GEM model pre- and post- CreER-induced recombination. **B,** Macroscopic images pre-, during, and post-4-HT application on a single mouse ear. Olympus MVX10. Scale bar, 500 μm. **C** and **D,** Macroscopic images with transmitted light (**C**) and tdTomato fluorescence (**D**) of tumor growth longitudinally over time on a single mouse ear, 2 to 9 weeks post-4-HT application. **E,** Tumor growth, measured by tumor depth, over time; $N \geq 12$. Error, 95% CI.

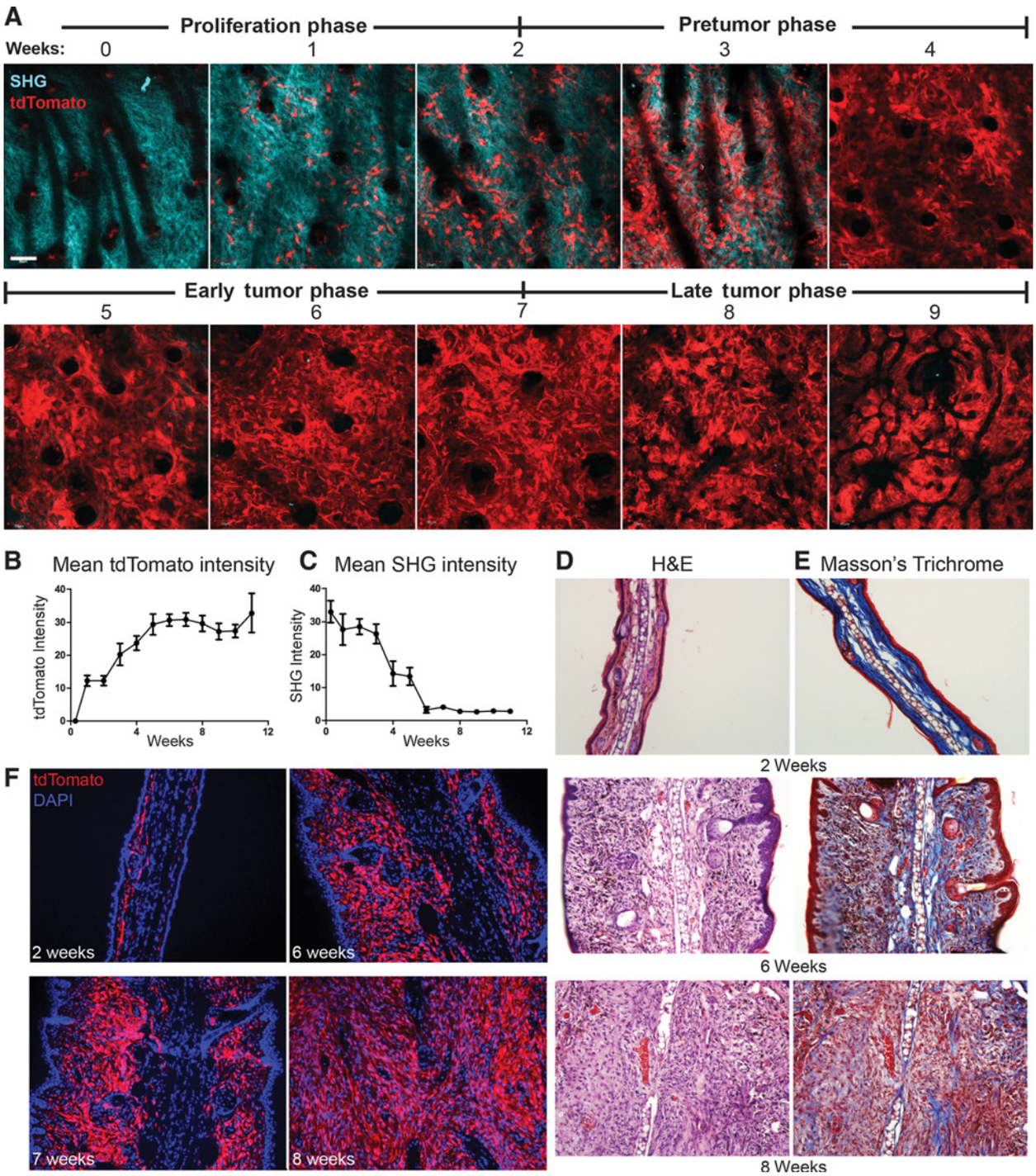

Figure 2.

Visualizing melanoma development over time with cellular resolution. **A,** Intravital multiphoton images of tdTomato$^+$ PBT melanoma development in the mouse ear over time; 0–9 weeks postapplication of 20 mmol/L 4-HT. SHG reveals bundled collagen within the dermis of the ear. Images show merged SHG and tdTomato channels. FV1000MPE; 1,050 nm; 4% laser power. Normalized average intensity of tdTomato signal (**B**) and SHG signal during tumor growth over time (**C**); $N \geq 12$. Error, 95% CI. Hematoxylin and eosin staining (**D**) and MT staining (**E**) of mouse ears 2, 6, and 8 weeks post-4-HT application. Olympus BX51; 10× objective; brightfield. **F,** Histology of tdTomato$^+$ tumor growth at 2, 6, 7, and 8 weeks postapplication of 20 mmol/L 4-HT. Images display merged DAPI and tdTomato channels. Olympus BX51; 20× objective.

patient response to therapy, we used this system to probe the longitudinal effects of the selective MEK1/2 inhibitor on melanoma behavior at the cellular and molecular levels.

Melanoma response to MEKi over time is heterogeneous

Standard of care for treating activated BRAF-mutant melanoma includes combination BRAFi (e.g., dabrafenib) and MEKi (e.g., trametinib) therapy (44). Mechanisms of resistance to BRAF inhibitors have been extensively characterized in both GEMs and humans. Herein we have focused on the response to the selective allosteric MEK1/2 inhibitor, trametinib (hereafter referred to as MEKi), which effectively inhibits both Ras and BRAF activation of the ERK pathway (27). To investigate how targeted MEKi therapy affects tumor behavior at the macroscopic and cellular levels in this model, we fed MEKi-containing chow to mice 8 to 9 weeks post-4-HT application, beginning at the late tumor phase, and serially imaged melanoma response to drug using intravital imaging. MEKi was incorporated into chow (Research Diets) with a daily dose of 0.3 mpk, and food intake was calculated using the Jackson Laboratory's Phenome Database, as in previous studies (45). Because tumor development is spatiotemporally controlled in our model, we were able to extend drug treatment and visualize both PBT melanoma response to MEKi and tumor regrowth (after 12 weeks on MEKi), mimicking extended tumor resistance to targeted therapy in patient settings.

Without drug treatment, tumors grew exponentially in a spatially defined region with relatively homogenous tdTomato expression throughout continued growth, compared with heterogeneous response over time on MEKi (Fig. 3A and B). All tumors responded quickly on MEKi treatment, however, with approximately 30% reduction in tumor size within the first week compared with control (Fig. 3C and D). Given enough time on therapy, disease progressed and tumors regrew, returning to their original size within 12 weeks. Tumor response was heterogeneous even at the macroscopic level, with some regions of persistent tdTomato signal and other regions devoid of fluorescence, which were re-populated with tdTomato$^+$ cells at late stages on MEKi (Fig. 3B, arrows). These results suggest evidence for both intrinsic and acquired functional resistance to MEKi in this model and mimic heterogeneous drug response.

MEKi induces epithelialization and intratumoral reorganization

We sectioned tumors at early and late stages on MEKi for histology and discovered decreased expression of vimentin, a mesenchymal marker, as well as an increase in E-cadherin via IHC (Fig. 3E and F). We also found changes in tumor cell organization and melanin expression over time through bright-field and fluorescence imaging (Supplementary Fig. S3A and S3B). Before drug treatment, tumor cells aggregated within the dermis but aligned with elongated and spindle-like morphologies closer to the cartilage boundary (Supplementary Fig. S3C, top). Early on MEKi, we identified intratumoral nests within the dermis, where tumor cells organized in a dense circular fashion (Supplementary Fig. S3C, middle). Tumor nests have been described as growth-promoting regions in melanoma, and at this stage on MEKi, they may indicate structures that promote therapeutic resistance (46). There was also a reduction in tdTomato$^+$ cells near the cartilage layer. At the late stage on MEKi during tumor regrowth, tumor nests were less obvious in the dermis, with a reemergence of melanoma cells again near the cartilage boundary (Supplementary Fig. S3C, bottom). Interestingly, tumor nests were only identified in regions of invasion through the cartilage boundary at the late stage on MEKi (Supplementary Fig. S3D). The density of tdTomato$^+$ melanoma was enhanced in the late MEKi stage compared with pretreatment, demonstrating that tumor regrowth was largely due to tumor cells themselves (Supplementary Fig. S3).

Tumor cells colocalize with bundled collagen during initial survival on MEKi

The ECM in tumors is highly dynamic, and deregulation of collagen crosslinking within the ECM has been shown to play a causative role in cancer pathogenesis (47, 48). We used our multiphoton intravital microscopy system to identify critical changes and dependencies between tumor cells and bundled collagen between early and late stages on MEKi. Before therapy, SHG signal was low, reflecting a loss or degradation of ECM in PBT tumors 9 weeks post-4-HT. However, MEKi treatment caused morphologic changes and reorganization of tumor cells as early as 3 days on drug (Fig. 4A). Strikingly, tdTomato strongly colocalized with SHG during this phase, suggesting that the bundled collagen within the dermis of the ear played a role in tumor cell survival on MEKi (Fig. 4A and B). After several weeks of continuous treatment, this spatial correlation between tumor cells and bundled collagen structures remained strong (Fig. 4A and B). Furthermore, the tdTomato$^+$ melanoma cell density increased over several weeks on MEKi, demonstrating microscopic tumor persistence prior to tumor regrowth.

In the late stage on MEKi (6–12 weeks), the correlation between tumor cells and bundled collagen structures diminished as the tumor regrew (Figs. 3D and 4). At this stage, we observed a loss in spatial correlation and colocalization between tdTomato and SHG signals, and we identified regions of tumor cells independent of collagen and vice versa (Fig. 4A, arrows). Through colocalization analysis between tdTomato and SHG signal, we were able to measure this loss in tumor cell association with bundled collagen over time on MEKi (Fig. 4B). This suggests that over time, as MEKi loses efficacy and melanoma becomes resistant, bundled collagen structures become less critical for tumor cell survival, which may be due to a significant change in tumor signaling or phenotype.

Classical IHC staining by hematoxylin and eosin and MT revealed that ECM deposition was greatly enhanced in the late stage compared with early on MEKi (Fig. 4C and D, blue stain). This suggests bundled collagen may play a significant role in tumor cell survival during the beginning of trametinib therapy. Although the ECM changed in character (deposition, location, concentration, distribution, organization), and bundled collagen increased during MEKi treatment, the dependency on bundled collagen for tumor cell survival at the individual cell level diminished as treatment continued, indicating a plastic relationship between ECM and tumor growth during drug response.

Kinome profiling of the MEKi response reveals potent and durable MEK1/2 inhibition and adaptive kinome reprogramming

Because we were able to visualize changes in drug response at the tumor cell level over time by intravital imaging, we sought to complement these insights by interrogating the molecular changes that occur over time on MEKi (Supplementary Fig. S4). To identify reprogramming events in the kinome in parallel with our imaging studies, we harvested MEKi-treated and control

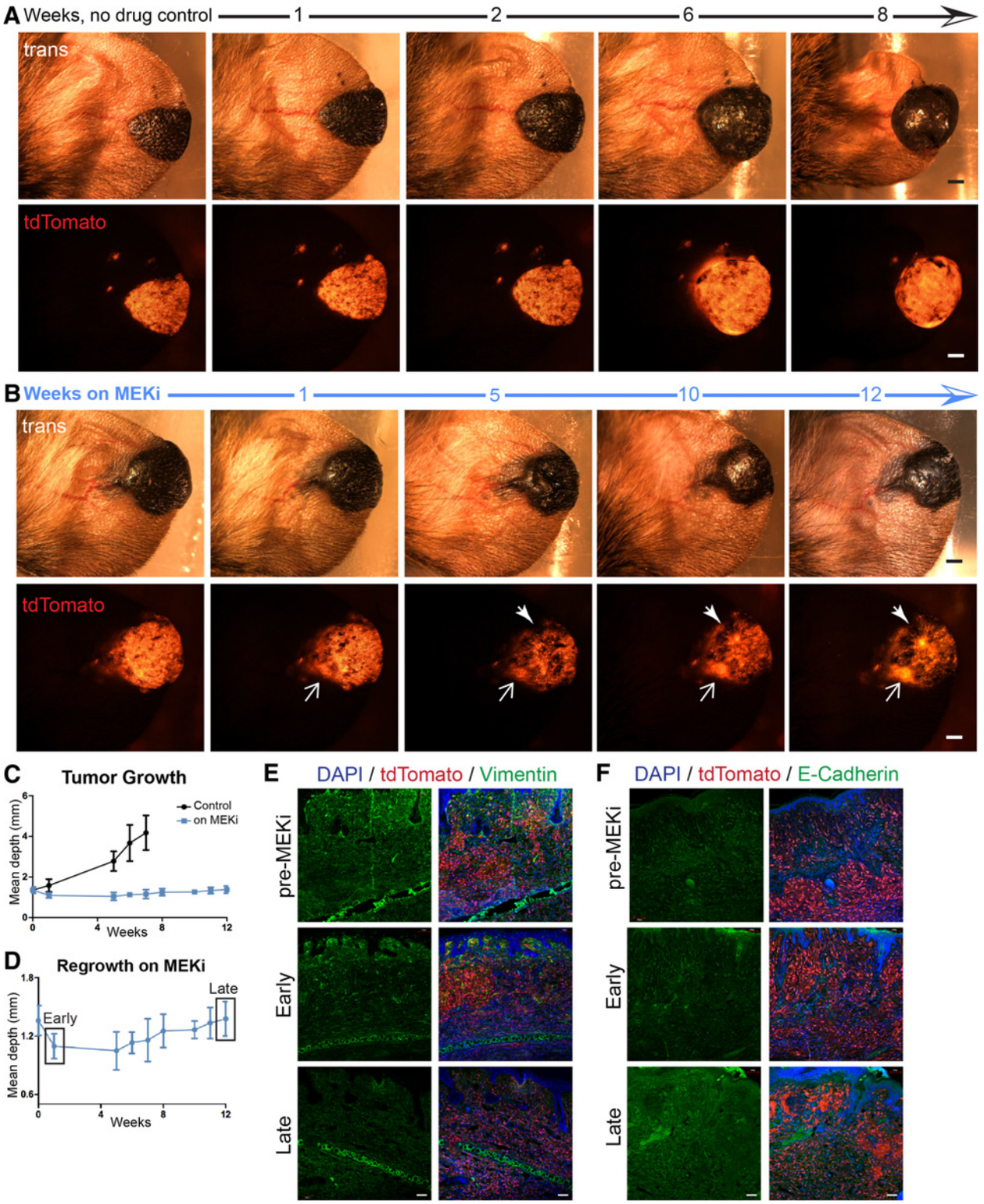

Figure 3.

Heterogeneous tumor response and epithelialization on MEKi over time. Macroscopic images of a PBT tumor without drug treatment 8, 9, 10, 14, and 16 weeks postapplication of 20 mmol/L 4-HT (**A**) and macroscopic images of a PBT tumor over time pre- and 1, 5, 10, and 12 weeks on trametinib therapy (**B**). Graphical representation of PBT tumor thickness/growth over time without MEKi trametinib treatment (**C**) and over time on MEKi therapy; $N \geq 4$. Error = 95% CI (**D**). Widefield images of IHC of PBT tumors pre-, at 1 week (early) and 7 weeks (late) on MEKi, stained with vimentin (**E**) and E-cadherin (**F**). Olympus FV1000, open pinhole; 20×.

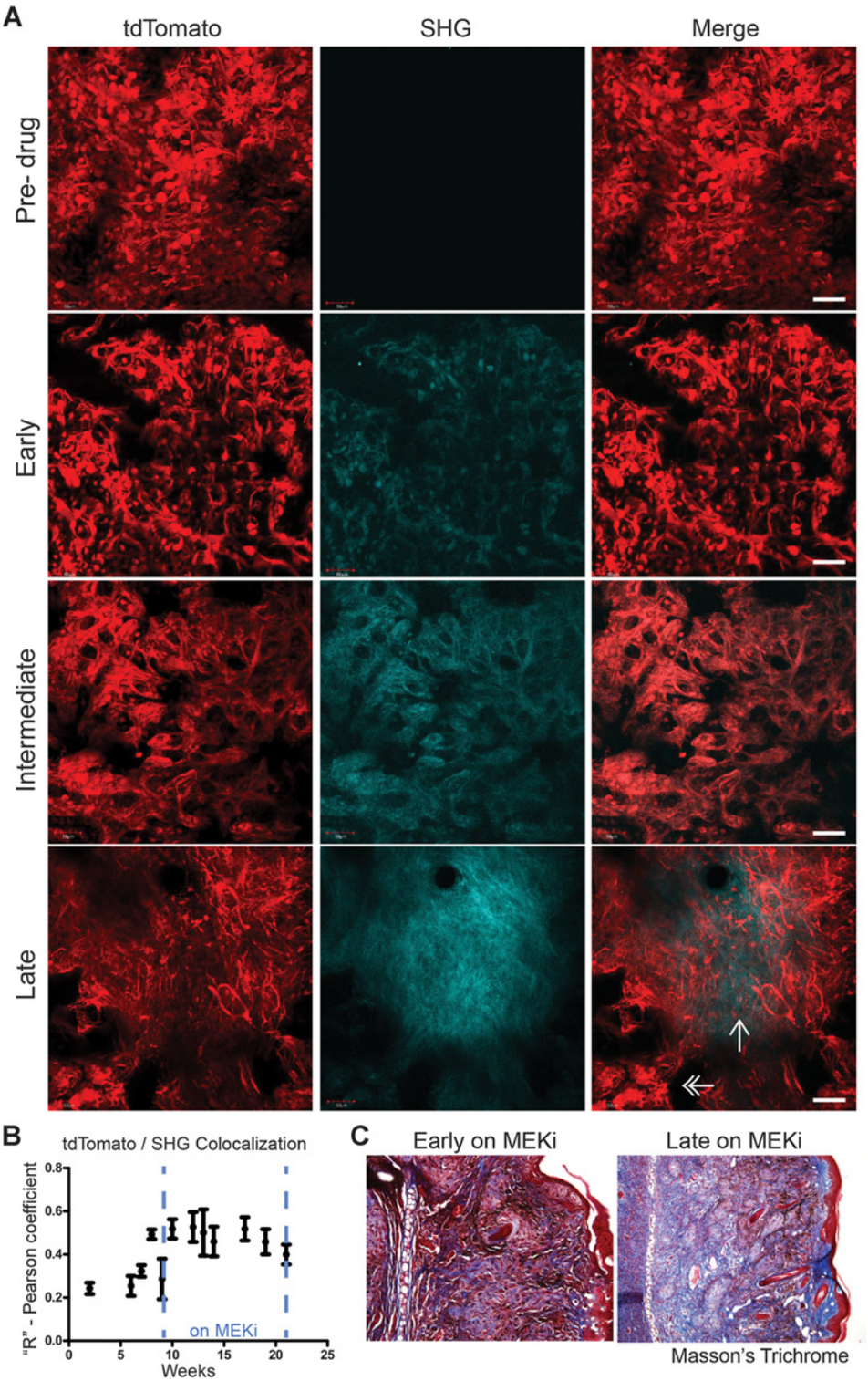

Figure 4.

Intravital imaging reveals a relationship between bundled collagen and tumor cells for survival on MEKi. **A,** Intravital multiphoton imaging of tdTomato^{+} PBT melanoma response to MEKi pretreatment and at early (3 days), intermediate (3.5 weeks), and late (9 weeks) stages on drug. Maximum intensity projections; FV1000MPE; 25×; 1,050 nm; 4% power. Scale bar, 50 μm. **B,** Average Pearson correlation coefficients for SHG and tdTomato signals over time on MEKi treatment; $N \geq 9$. Error, 95% CI. **C,** MT staining of histologic slices of PBT melanoma at early and late time points (1 and 7 weeks) on MEKi. Blue signal represents intratumoral ECM and bundled collagen.

tumors and performed molecular analysis of tumor response. We used a chemical proteomics approach (multiplexed-inhibitor bead affinity chromatography coupled with MS, MIB/MS) to assess the state of the kinome in our model. The adaptive response to targeted kinase inhibitors can lead to dramatic alterations in signaling and ultimately to drug resistance and tumor progression (49–51). We have previously used MIB/MS to characterize the adaptive response leading to therapeutic resistance to MEK inhibition in triple-negative breast cancer and lapatinib in $HER2^+$ breast cancer (29, 52). The affinity purification involves a mixture of type I kinase inhibitors to selectively enrich for kinases based on their activation state, abundance, and affinity for the inhibitors. Untreated tumors and tumors from mice treated for 1 week (early) or 12 weeks (late) on MEKi were harvested, snap-frozen, and processed for MIB/MS (Fig. 5A). As predicted, loss of MEK1/2 MIB binding (as determined by LFQ intensity) was dramatic compared with untreated control tumors and persisted throughout the duration of the experiment (Fig. 5B). The MIB binding loss of BRAF and ERK1/2 was also readily observed by LFQ intensity (Supplementary Figs. S5A–S5C). These observations confirmed that tumors from the trametinib-treated mice displayed MEK inhibition coincident with the overall tumor depth decrease.

To gain insight into the global kinome response to MEK inhibition, the kinome data were processed with Perseus software and hierarchical clustering of the $\log_2$-transformed LFQ intensities was performed (Fig. 5C). Notably, the majority of kinases exhibited a comparative loss of binding in response to trametinib related to the growth arrest and tumor shrinkage (Fig. 5C, inset). Despite the potent inhibition of MEK, a subset of kinases displayed a pattern of increased MIB binding over time. These kinases included the RTKs c-KIT and Ephrin type-A receptor 1 (EPHA1), the metabolic kinase FN3K, PTK6, the stress-associated kinase CDK5, and B lymphoid kinase (BLK). Although a degree of tumor heterogeneity could be observed in the untreated and early time points, the late group appeared more similar in global kinome behavior. This observation was corroborated by principal component analysis of the kinome profile (Supplementary Fig. S5D). To visualize the magnitude and significance of the kinome changes, volcano plots were generated for the early and late MEKi-treated tumors relative to the untreated control group (Fig. 5D and E). As expected, we saw significant loss in MIB binding of MEK1 and MEK2. In contrast, kinases such as c-KIT, FGFR3, and BLK were most dramatically increased in response to MEKi. These observations were confirmed via Western blot analysis of tumor lysates (Fig. 5F), including loss of phospho-ERK1/2 and a decrease in total PDGFRβ. In addition, tdTomato levels were comparable across all of the tumors by Western blot analysis (Supplementary Fig. S5E). These experiments demonstrate the feasibility of chronologic kinome evaluation in our melanoma model and demonstrate the plasticity of the kinome, even in response to a potent and selective MEKi. The adaptive kinome response allows a reprogramming of melanoma signaling for the onset of resistance to MEKi.

Transcriptome analysis reveals a phenotypic state change with enhanced epithelial signature in response to MEKi

To assay changes in gene expression throughout MEKi treatment, we utilized sections of snap-frozen tumors harvested at early and late time points of drug treatment for RNA-seq analysis and compared expression changes with the adaptive kinome response, measured by MIB/MS. As shown in Fig. 6A, hierarchical clustering of kinome gene expression in response to MEK inhibition revealed substantial and distinct changes at both early and late time points compared with untreated tumors. To identify differentially expressed kinases, we performed DESeq2 comparing the early and late time points to control tumors and visualized the genes in volcano plots (32). After one week on MEKi, the expression of numerous kinases was dramatically altered (Fig. 6B). Expression of *Mek1*/*Map2k1* and *Mek2*/*Map2k2* was significantly decreased with *Mek1* levels reduced more significantly than *Mek2*. Other kinases with diminished expression included the poorly characterized serine/threonine kinase *Stk32a*, *Cdk18*, *Akt3*, *Epha3*, and *Alk*. In contrast, the tumors harvested after 1 week of treatment displayed increased expression of the fibroblast growth factor receptors *Fgfr2* and *Fgfr3*, as well as *Rps6ka1 (p90Rsk)* and *Ddr1*, which we have observed in previous *in vitro* studies (52).

At the late time point, *Mek1*/*Map2k1* and *Mek2*/*Map2k2* were not significantly altered (Fig. 6C). In contrast, the expression of kinases including *Cdk18*, *Alk*, *Akt3*, and *Stk32a* was reduced more significantly and to a greater degree over the course of trametinib treatment. Another kinase with increased gene expression at the late time point included *Ntrk1*, neurotrophic receptor tyrosine kinase, which is important for neuronal development and survival and may play a similar role in melanoma (53). In addition, expression of the nonreceptor Src-related tyrosine kinase *Srms*, thought to play a role in keratinocyte proliferation, was increased at the late time point (Fig. 6). Distinct from the early time point, the expression of lymphocyte kinases *Itk* and *Zap70* was increased with MEK inhibition. Collectively, chronic treatment with MEKi led to tumor persistence and regrowth that involved a reprogramming of specific kinase expression observed in both early and late time points.

To directly compare the MIB/MS kinome profiles with RNA-seq expression data, we plotted the fold-changes observed in kinome by each assay (Fig. 6D and E). At both the early and late time points, the inhibition of Mek1 and Mek2 was almost exclusively pharmacologic, as determined by loss of MIB binding. In contrast, the loss of *Cdk18*, *Epha3*, *Epha7*, and *Stk32a* was observed at the transcript level correlating with loss of functional MIB binding. The RTKs *Met* and *Epha1* were found to increase by both RNA-seq and MIB binding, whereas expression of the RTK *Kit* was only significantly increased in the early stage but displayed sustained functional MIB binding throughout the course of MEKi treatment (Fig. 6D and E). The B lymphocyte kinase, Blk, exhibited increased binding at the late time point but no change in gene expression. Together, the RNA-seq and kinome data indicate a transcriptional reprogramming of the kinome that results in an adaptive change in functional kinases demonstrated by the ability to capture kinases with MIBs.

As an additional approach to global analysis, we used pathway analysis of gene expression signatures (35). Using a panel of previously published gene signatures derived from human transcriptional profiles, pathway signature scores were derived from the mouse tumors using the shared Homologene ID (Fig. 6F). Clustering of the pathway signatures readily illuminated five distinct patterns of pathway activity (Fig. 6F; Supplementary Figs. S6A–S6D). High pathway signature scores for cluster 1 (related to mammary stem cells, basal-type breast cancer, and fibroblasts) were observed in the untreated control tumors but not in MEKi-treated tumors. Thus, the tumors appeared to shift from mesenchymal-like to epithelial-like expression patterns after 1 week on MEKi. In addition, signature scores for pathways associated with

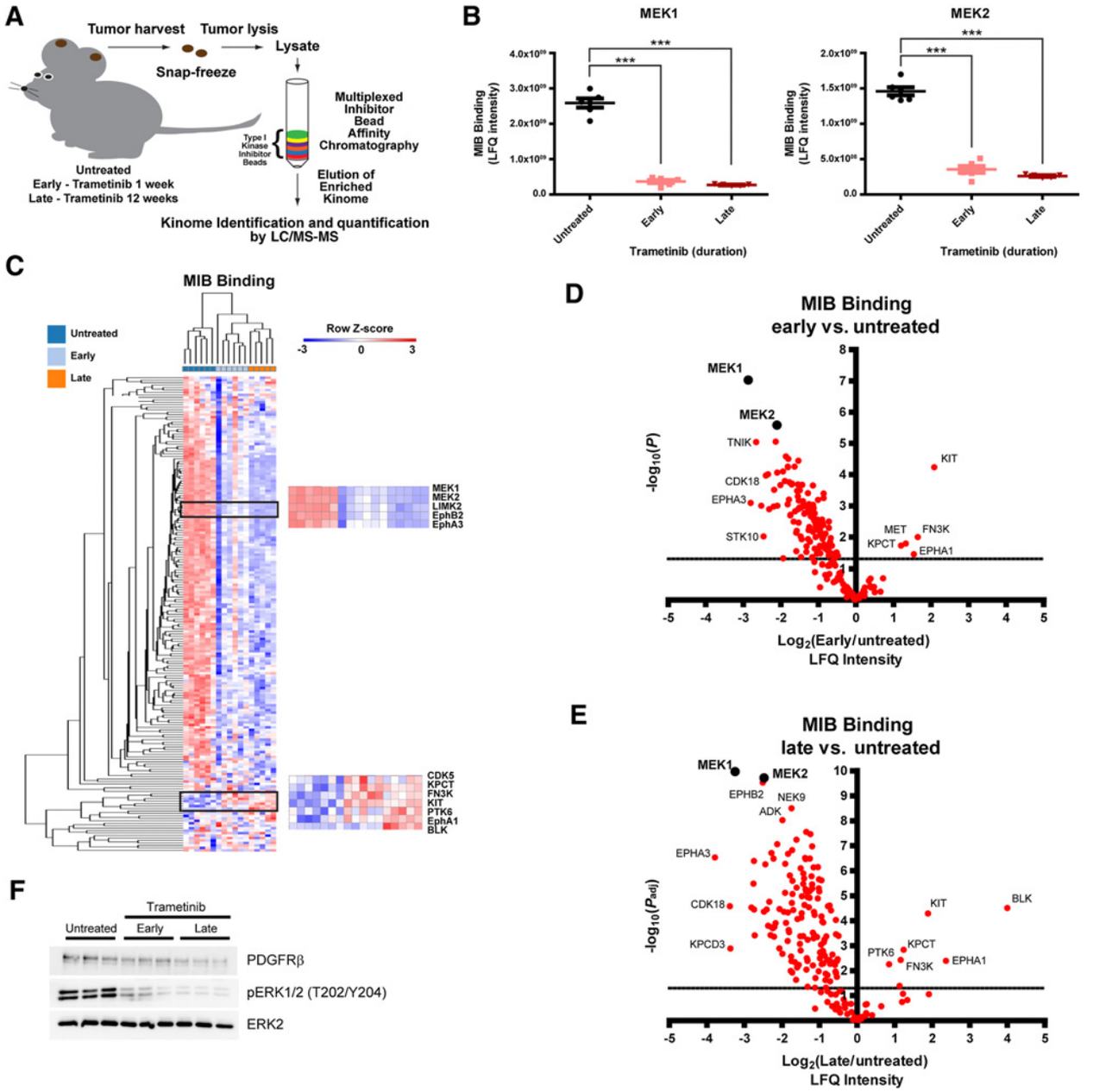

Figure 5.

Adaptive kinome response to chronic and potent MEK inhibition. **A,** Schematic representation of experimental MIB/MS workflow. **B,** MIB binding (LFQ intensities) for MEK1 and MEK2 from untreated, early, and late tumors. ***, $P < 0.001$. **C,** Hierarchical clustering displayed as a heat map of mean-centered, $\log_2$-transformed LFQ intensities (MIB binding) from untreated, early, and late tumors as in **A**. Select panels are indicated and labeled with kinases by row. **D,** Volcano plot showing $\log_2$-fold change MIB binding (LFQ intensity) for early versus untreated tumors plotted against the $-\log_{10} P$ value (FDR = 0.05). Dotted line, $P = 0.05$. **E,** Volcano plot showing $\log_2$-fold change MIB binding (LFQ intensity) for late versus untreated tumors plotted against the $-\log_{10} P$ value (FDR = 0.05). Dotted line, $P = 0.05$. **F,** Western blots for untreated, early, and late tumors as in **A**. ERK2 was used as a loading control.

immune response (e.g., T-cell, B-cell, CD8) increased in response to MEKi, and indicative of prosurvival signaling, PI3K and AKT pathway scores were also increased over time. Despite some heterogeneity observed in each group, the signature scores for EMT_up and EMT_down were decreased and increased, respectively, over time on MEKi. Thus, the global pathway analysis corroborated the persistent survival of tdTomato$^+$ tumor cells and supported a shift to an epithelial state and immune response during treatment.

As the pathway analysis suggested a transcriptional response to an epithelial phenotype, we explored the relative expression levels of a subset of epithelial-mesenchymal transition (EMT)-associated

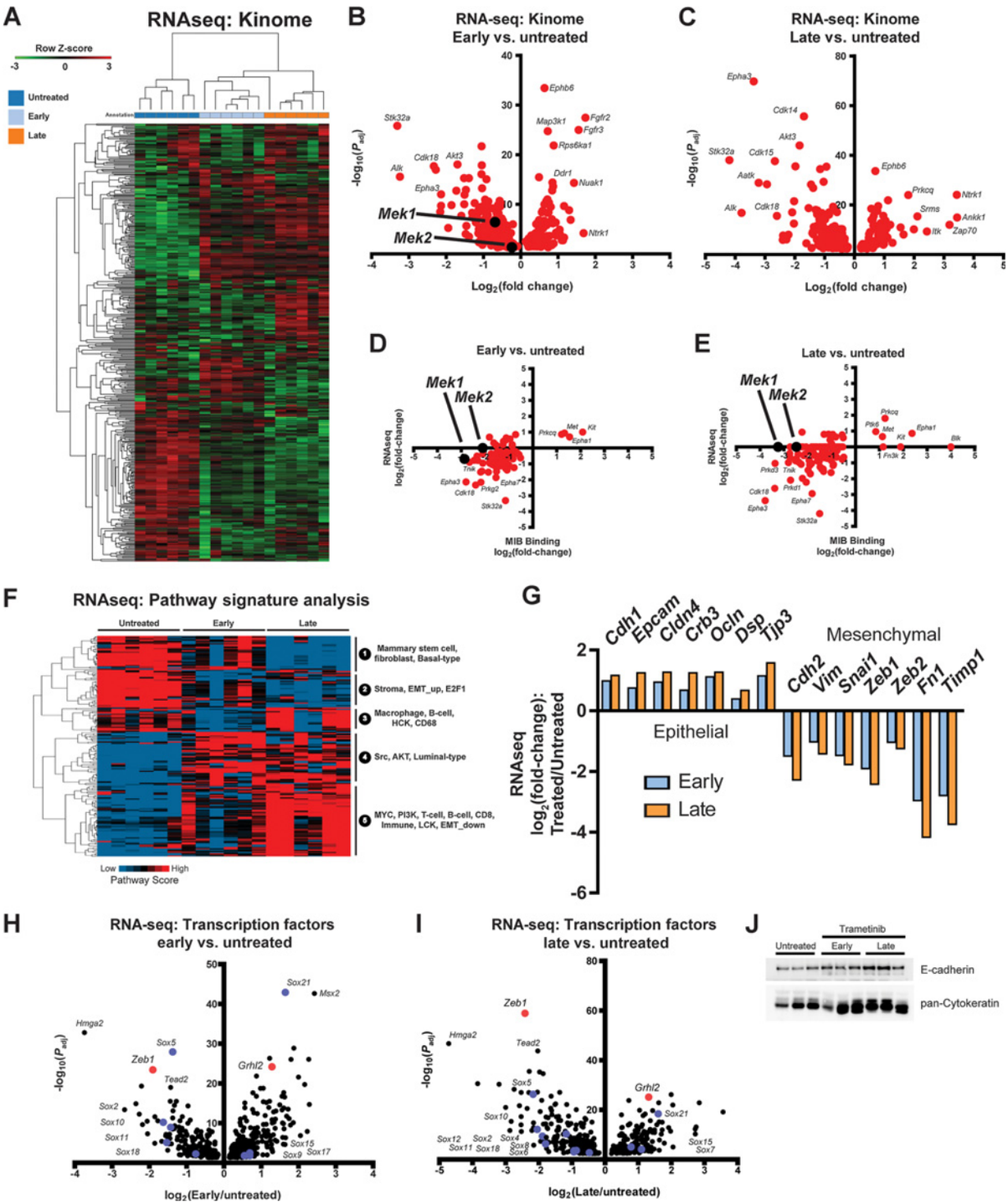

Figure 6.

Transcriptome profiling reveals dramatic mesenchymal-to-epithelial phenotypic shift in response to trametinib. **A,** RNA-seq analysis of untreated, early, and late tumors as $\log_2$-transformed RSEM normalized gene counts. Hierarchical clustering displayed as a heat map of the mean-centered mouse kinase genes. **B,** Volcano plot showing $\log_2$-fold change (RNA-seq) for early versus untreated tumors plotted against the $-\log_{10}$-adjusted *P* value (FDR = 0.05) as determined by DESeq2. Dotted line, $P = 0.05$. **C,** Volcano plot showing $\log_2$-fold change (RNA-seq) for late versus untreated tumors plotted against the $-\log_{10}$-adjusted *P* value (FDR = 0.05) as determined by DESeq2. Dotted line, $P = 0.05$. **D,** Log_2 LFQ intensities (MIB binding) and $\log_2$ RNA-seq expression changes (early vs. untreated) are plotted for kinases quantified by MIB/MS. **E,** Log_2 LFQ intensities (MIB binding) and $\log_2$ RNA-seq expression changes (late vs. untreated) are plotted for kinases quantified by MIB/MS. **F,** RNA-seq data from untreated, early, and late tumors were used for pathway signature analysis and clustered. Representative signatures from each cluster are indicated at right. **G,** Log_2-fold change as determined by DESeq2 for select genes involved in EMT. **H,** Volcano plot as in **B** for transcription factor genes. **I,** Volcano plot as in **C** for transcription factor genes. **J,** Western blots for indicated proteins from untreated, early, and late tumors.

genes (Fig. 6G). Genes associated with epithelial phenotype, such as E-cadherin, were significantly increased in response to MEKi whereas those associated with mesenchymal phenotype were reduced. Changes in these EMT-associated genes were sustained during MEKi therapy in the early and late treatment groups. Gene list enrichment analysis by Enrichr reinforced this finding, as genes significantly upregulated at early and late time points were most enriched in the "Epithelium" gene set for Mouse Gene Atlas (Supplementary Figs. S6E-TRAMETINIB).

Given the dramatic changes in the transcriptome observed in our model in response to MEKi, we surmised that lineage-specific transcription factors might drive the observed phenotypic shift. Therefore, we investigated the mouse transcription factors as a discrete gene subset (Fig. 6H and I). The *Sox* family of transcription factors are critical players in neural crest development and have been implicated in melanomagenesis (54, 55). In response to MEKi, we observed a significant upregulation of *Sox21* and downregulation of *Sox5* and *Sox10*. Furthermore, two of the most significantly altered transcription factors at both time points were *Zeb1* and *Grhl2* (Grainy-head-like 2). Interestingly, *Zeb1* and *Grhl2* have been demonstrated to participate in an intricate reciprocal regulatory feedback loop that governs EMT in breast cancer (56). As the transcriptome analysis indicated a shift to an epithelial-like phenotype in the persistent tumors, we performed immunoblotting and confirmed that E-cadherin (CDH1) and pan-Cytokeratin increased in response to MEKi (Fig. 6J).

Analysis of the transcriptome revealed that the adaptive kinome reprogramming and collagen reorganization occur in concert to promote persistence of melanoma cells for long-term survival on MEKi. In addition, although EMT has been characterized as a potential mechanism for resistance to BRAFi, our gene expression analysis suggests the opposite, with increased epithelial signatures in drug-treated tumors compared with control.

Modeling BRAFi and MEKi combination therapy

Although these studies focus on the singular effects of MEK inhibition, we also utilized the combinatorial treatment of dabrafenib and trametinib that has provided more durable clinical responses when compared with BRAFi alone. Intravital imaging of tumors on BRAFi/MEKi combination therapy revealed a similar pattern in stromal collagen plasticity; however, regions of collagen independent of tumor cells were visualized as early as 2 weeks on drug treatment (Fig. 7A). As anticipated, treatment with BRAFi/MEKi caused tumor shrinkage, similar to MEKi alone, but with sustained and prolonged growth inhibition (Fig. 7B).

Untreated tumors and tumors treated for 1 week (early) or 5–12 weeks (late) with BRAFi/MEKi were harvested. By MIB/MS analysis of the functional kinome, treated tumors segregated in response to BRAFi/MEKi (Fig. 7C; Supplementary Fig. S7A and S7B). MEK inhibition was consistently observed (sufficient unique peptides for BRAF were not detected for quantification) and numerous RTKs exhibited increased binding—*Ddr1*, *Met*, *Ptk6*, *EphA1* (Supplementary Fig. S7A–S7B). However, the early and late treatment groups for BRAFi/MEKi were less distinguishable from one another by principal component analysis than in response to MEKi alone (Supplementary Fig. S7C). This observation was consistent with the reported durability of combined BRAF and MEK inhibition and with the significant tumor regression we observed in our model throughout the experiment.

RNA-seq was also performed on tumor samples, and dramatic alterations in kinome expression patterns were observed (Fig. 7D and E; Supplementary Fig. S7D). The kinome expression changes were compared to the MIB/MS kinome profiles. Although MEK1 and MEK2 displayed significant loss of MIB binding consistent with MEKi treatment with minimal change in expression, kinases including *Ddr1*, *Fgfr2*, and *Ptk6* exhibited increased expression levels in parallel with enhanced functional MIB binding in response to BRAFi/MEKi. As with single-agent MEKi, analysis of transcription factor expression in response to BRAFi/MEKi revealed increased *Grhl2* and decreased *Zeb1* expression and dynamic shifts in the expression of Sox transcription factors (Supplementary Fig. S7E and S7F). Pathway signature analysis of the RNA-seq data substantiated the phenotypic shift toward a more epithelial-like phenotype (decrease in EMT_up signature over time) and evidence of immune infiltration (increase T-cell signature) (Fig. 7F). Western blots from mouse melanoma tumors indicated that treatment with BRAFi/MEKi led to an expected decrease in phospho-MEK1/2 not seen with MEKi alone. Although BRAF and phospho-MEK1/2 levels rebounded at the late time point, signaling to phosphoERK1/2 was not fully restored, consistent with the loss of MEK MIB binding.

To validate our observation of alterations in EMT factors and Sox lineage transcription factors, we examined clinical data and human melanoma cell lines. Analysis of clinical data in which patients received BRAFi or BRAFi/MEKi revealed that the Sox family of transcription factors are highly dynamic EDT and at progression in response to MAPK pathway inhibition (Supplementary Fig. S7G). Furthermore, analysis of a panel of human melanoma cell lines exhibited heterogeneity at baseline and in their response to BRAFi/MEKi in EMT markers, Sox transcription factors, and RTKs (Fig. 7G). Our model exhibited behavior strongly similar to the human cell line SK-MEL-100—an RTK response involving *c-Kit* and a shift toward an epithelial-like phenotype, highlighted by increased expression of *E-cadherin* and decreased *Beta-catenin*. Collectively, these data reinforced our findings with single agent MEKi that the tumors underwent adaptive changes to combined BRAFi/MEKi over time and displayed phenotypic changes and persistent survival.

Discussion

We developed a highly localized 4-HT application method in an inducible GEM model that achieved reproducible spatiotemporal control of melanoma development on the mouse ear. We reproducibly tracked melanoma development from initial stages through advanced tumorigenesis, and then used long-term longitudinal studies to study tumor response to therapy, closely mimicking clinical response in patient settings.

Our intravital imaging approaches allowed us to observe tumorigenesis from the single cell stage *in vivo*. We identified several reproducible phases of melanoma development. Early on, we visualized the development of clonal populations of melanoma cells directly in the dermis, which became densely packed pretumorous lesions that spread radially throughout the dermis, as it occurs in humans. By 2 months post-4-HT application, melanoma grew vertically within the dermis to form palpable and spatially defined tumors.

Through long-term longitudinal studies on MEKi in our melanoma model, we discovered that intratumoral reorganization of melanoma cells and bundled collagen, along with enhanced expression of epithelial markers, played a significant role in tumor cell survival on drug. The SHG signal tightly correlated with

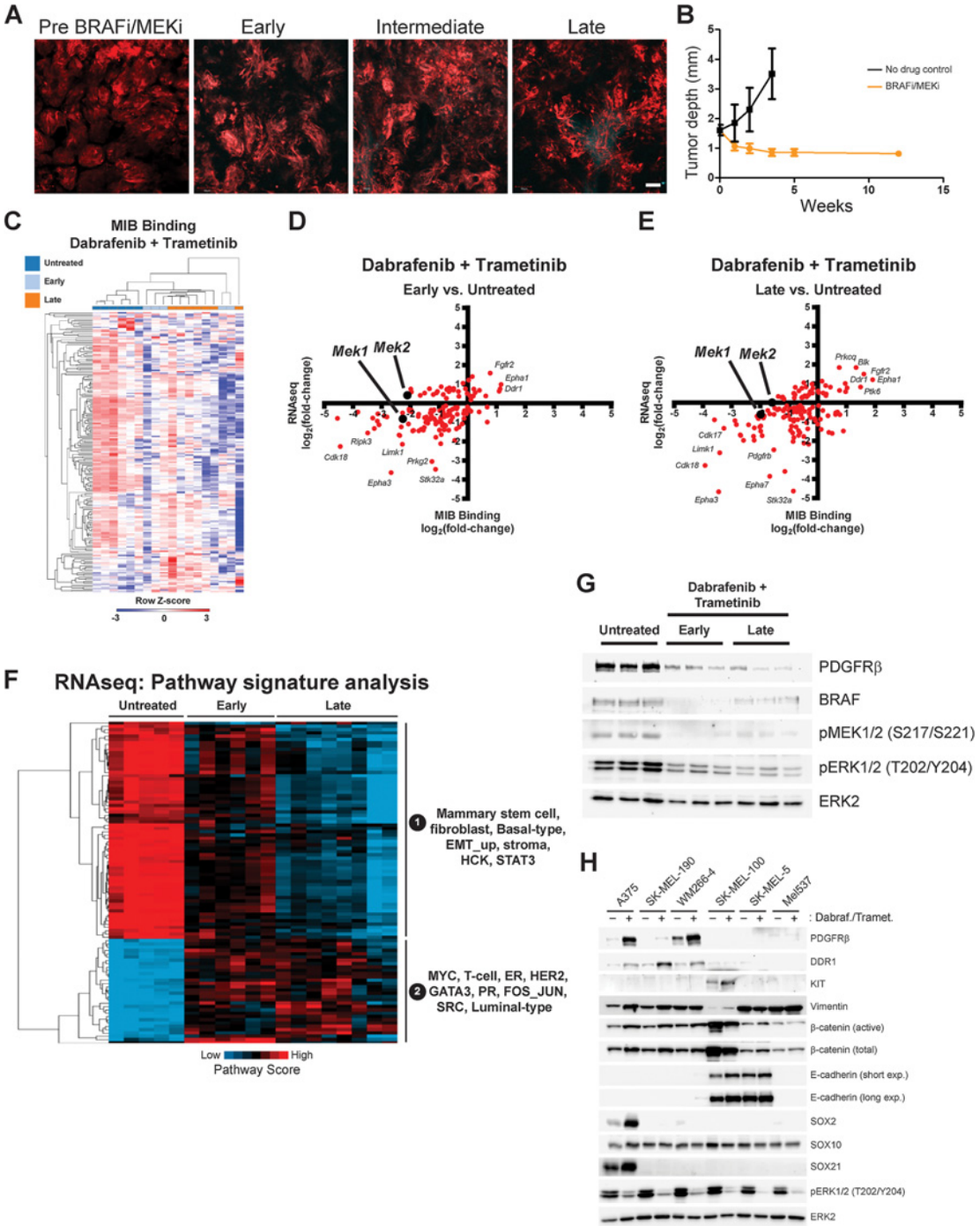

Figure 7.

Combined inhibition of MEKi and BRAFi also reveals an EMT_down signature and kinome reprogramming in persistent melanoma. **A,** Intravital multiphoton imaging of tdTomato$^+$ PBT melanoma response to BRAFi/MEKi combination pretreatment and at early (5 days), intermediate (2 weeks), and late (11 weeks) stages on drug. Maximum intensity projections; FV1000MPE; 25×; 1,050 nm; 4% power. Scale bar, 50 μm. **B,** Graphical representation of PBT tumor thickness over time with and without BRAFi/MEKi treatment over time. $N \geq 6$, except 12-week $N = 2$. Error, 95% CI. **C,** Hierarchical clustering displayed as a heat map of mean-centered, $\log_2$-transformed LFQ intensities (MIB binding) from untreated, early, and late tumors as in Fig. 6A. **D,** $\log_2$ LFQ intensities (MIB binding) and $\log_2$ RNA-seq expression changes (early vs. untreated) are plotted for kinases quantified by MIB/MS. **E,** $\log_2$ LFQ intensities (MIB binding) and $\log_2$ RNA-seq expression changes (late vs. untreated) are plotted for kinases quantified by MIB/MS. **F,** RNA-seq data from untreated, early, and late tumors were used for pathway signature analysis and clustered. Representative signatures from each cluster are indicated at right. **F,** Western blots for untreated, early, and late tumors as in **A**. ERK2 was used as a loading control.

tdTomato$^+$ cells at early treatment stages, suggesting a model of dependency on bundled collagen for initial tumor cell survival. In the late stage on MEKi, however, this correlation was abrogated, with heterogenous regions of melanoma cells present independent of collagen; graphically represented in Supplementary Fig. S8. Structural intratumoral differences at different stages on drug, like the presence of tumor nests in regions of invasion across the cartilage boundary at the late stage on MEKi, could support protective mechanisms that enable long-term survival on drug. In addition, although direct interaction with bundled collagen matrix was reduced in the late stage on MEKi, there is more collagen within tumors at this stage overall, compared with pretreatment. These results suggest that the stiffening of tumors due to enhanced collagen deposition and tumor cell reorganization over time may promote resistance to targeted therapy.

Furthermore, spatiotemporal control of tumor growth enabled us to perform a longitudinal and comprehensive view of molecular plasticity on drug *in vivo*. Analysis of our MIB/MS data revealed enhanced activity of the collagen binding receptor DDR1 at the early stage on MAPKi, promoting the idea that collagen promotes tumor cell survival against therapy. Although phenotype switching via "EMT" has previously been described as a means to promote drug resistance; instead, we find evidence that "MET" progression appears to enhance survival of melanoma against MAPKi. Notably, a novel "keratin-high" and epithelial-like subclass of melanoma that correlated with poor prognosis was recently described by the TCGA analysis of human cutaneous melanoma (57). Comparing mRNA-seq and MIB/MS data of melanoma tumors in late versus early stages on drug, we have identified c-KIT, EPHA1, CDK5, BLK, PTK6, and FGFR2/3 as potential drivers of functional resistance to MEKi in this model. These finding were recapitulated in combination BRAFi/MEKi-treated tumors and consistent with the heterogeneity of responses seen in patients and human cell line models.

By using a combination of novel approaches in our model system, we set the stage for new discoveries and understanding about tumor biology and therapeutic response. Coupling our imaging studies with transcriptome and kinome reprogramming analysis enables direct interrogation of tumor plasticity *in vivo* during drug response and identification of properties and potential therapeutic targets that promote resistance. Using these novel approaches, we have developed a model that enables direct observation of endogenous tumor development, tumor heterogeneity, and plastic response to targeted therapy at the endogenous cell level *in situ*. These methods will advance our basic understanding of the cellular processes involved in disease progression, increase the utility of existing and future GEM models, and aid in the testing of new therapeutics for malignant melanoma.

Disclosure of Potential Conflicts of Interest

No potential conflicts of interest were disclosed.

Authors' Contributions

Conception and design: G.L. Johnson, J.E. Bear
Development of methodology: N.E. Sharpless
Acquisition of data (provided animals, acquired and managed patients, provided facilities, etc.): H.E. Brighton, S.P. Angus, T. Bo, J. Roques, A.C. Tagliatela, D.B. Darr
Analysis and interpretation of data (e.g., statistical analysis, biostatistics, computational analysis): H.E. Brighton, S.P. Angus, K. Karagoz, N. Sciaky, M.L. Gatza, N.E. Sharpless, J.E. Bear
Writing, review, and/or revision of the manuscript: H.E. Brighton, S.P. Angus, K. Karagoz, M.L. Gatza, N.E. Sharpless, G.L. Johnson, J.E. Bear
Administrative, technical, or material support (i.e., reporting or organizing data, constructing databases): D.B. Darr, J.E. Bear
Study supervision: G.L. Johnson, J.E. Bear

Acknowledgments

This work was supported by HHMI funds to J.E. Bear, Melanoma Research Alliance (grant no. 310979 to G.L. Johnson), R00-CA166228, and V Foundation for Cancer Research (V2016-13 to M.L. Gatza; RO1 CA185353 to N.E. Sharpless).

The costs of publication of this article were defrayed in part by the payment of page charges. This article must therefore be hereby marked *advertisement* in accordance with 18 U.S.C. Section 1734 solely to indicate this fact.

Received June 9, 2017; revised October 6, 2017; accepted November 10, 2017; published OnlineFirst November 27, 2017.

References

1. Mehnert JM, Kluger HM. Driver mutations in melanoma: lessons learned from bench-to-bedside studies. Curr Oncol Rep 2012;14:449–457.
2. Hodis E, Watson IR, Kryukov GV, Arold ST, Imielinski M, Theurillat JP, et al. A landscape of driver mutations in melanoma. Cell 2017;150: 251–263.
3. Wan PTC, Garnett MJ, Roe SM, Lee S, Niculescu-Duvaz D, Good VM, et al. Mechanism of activation of the RAF-ERK signaling pathway by oncogenic mutations of B-RAF. Cell 2004;116:855–867.
4. Flaherty KT, Robert C, Hersey P, Nathan P, Garbe C, Milhem M, et al. Improved survival with MEK inhibition in BRAF-mutated melanoma. N Engl J Med 2012;367:107–114.
5. Long GV, Stroyakovskiy D, Gogas H, Levchenko E, de Braud F, Larkin J, et al. dabrafenib and trametinib versus dabrafenib and placebo for Val600 BRAF-mutant melanoma: a multicentre, double-blind, phase 3 randomised controlled trial. Lancet 2017;386:444–451.
6. Wellbrock C, Arozarena I. The complexity of the ERK/MAP-kinase pathway and the treatment of melanoma skin cancer. Front Cell Dev Biol 2016;4:33.
7. Karimkhani C, Gonzalez R, Dellavalle RP. A review of novel therapies for melanoma. Am J Clin Dermatol 2014;15:323–337.
8. James L, Ascierto PA, Dréno B, Atkinson V, Liszkay G, Maio M, et al. Combined vemurafenib and cobimetinib in BRAF-mutated melanoma. N Engl J Med 2014;371:1867–1876.
9. Spagnolo F, Ghiorzo P, Queirolo P. Overcoming resistance to BRAF inhibition in BRAF-mutated metastatic melanoma. Oncotarget 2014;5: 10206–21.
10. Manzano JL, Layos L, Bugés C, de los LGil M, Vila L, Martínez-Balibrea E, et al. Resistant mechanisms to BRAF inhibitors in melanoma. Ann Transl Med 2016;4:237.
11. Lu H, Liu S, Zhang G, Bin Wu, Zhu Y, Frederick DT, et al. PAK signalling drives acquired drug resistance to MAPK inhibitors in BRAF-mutant melanomas. Nature 2017;550:133–6.
12. Usary J, Zhao W, Darr D, Roberts PJ, Liu M, Balletta L, et al. Predicting drug responsiveness in human cancers using genetically engineered mice. Clin Cancer Res 2013;19:4889 LP–4899.
13. Hoek KS, Eichhoff OM, Schlegel NC, Döbbeling U, Kobert N, Schaerer L, et al. *In vivo* switching of human melanoma cells between proliferative and invasive states. Cancer Res 2008;68:650 LP–656.
14. Kemper K, de Goeje PL, Peeper DS, van Amerongen R. Phenotype switching: tumor cell plasticity as a resistance mechanism and target for therapy. Cancer Res 2014;74:5937 LP–5941.
15. Sanchez-Laorden B, Viros A, Girotti MR, Pedersen M, Saturno G, Zambon A, et al. BRAF inhibitors induce metastasis in RAS mutant or inhibitor-resistant melanoma cells by reactivating MEK and ERK signaling. Sci Signal 2014;7:ra30 LP–ra30.

16. Roesch A.Tumor heterogeneity and plasticity as elusive drivers for resistance to MAPK pathway inhibition in melanoma. Oncogene 2015;34: 2951–7.
17. Straussman R, Morikawa T, Shee K, Barzily-Rokni M, Qian ZR, Du J, et al. Tumour micro-environment elicits innate resistance to RAF inhibitors through HGF secretion. Nature 2012;487:500–504.
18. Smith MP, Sanchez-Laorden B, O'Brien K, Brunton H, Ferguson J, Young H, et al. The immune microenvironment confers resistance to MAPK pathway inhibitors through macrophage-derived TNFα. Cancer Discov 2014;4: 1214 LP–1229.
19. Menzies AM, Haydu LE, Carlino MS, Azer MW, Carr PJ, Kefford RF, et al. Inter- and intra-patient heterogeneity of response and progression to targeted therapy in metastatic melanoma. PLoS One 2014;9:1–9.
20. Egeblad M, Nakasone ES, Werb Z. Tumors as organs: complex tissues that interface with the entire organism. Dev Cell 2017;18:884–901.
21. Hofschröer V, Koch KA, Ludwig FT, Friedl P, Oberleithner H, Stock C, et al. Extracellular protonation modulates cell-cell interaction mechanics and tissue invasion in human melanoma cells. Sci Rep 2017;7:42369.
22. Sandri S, Faião-Flores F, Tiago M, Pennacchi PC, Massaro RR, Alves-Fernandes DK, et al. Vemurafenib resistance increases melanoma invasiveness and modulates the tumor microenvironment by MMP-2 upregulation. Pharmacol Res 2016;111:523–33.
23. Hirata E, Girotti MR, Viros A, Hooper S, Spencer-Dene B, Matsuda M, et al. Intravital imaging reveals how BRAF inhibition generates drug-tolerant microenvironments with high integrin β1/FAK signaling. Cancer Cell 2015;27:574–88.
24. Cox TR, Erler JT. Remodeling and homeostasis of the extracellular matrix: implications for fibrotic diseases and cancer. Dis Model Mech 2011;4:165 LP–178.
25. Madisen L, Zwingman TA, Sunkin SM, Oh SW, Zariwala HA, Gu H, et al. A robust and high-throughput Cre reporting and characterization system for the whole mouse brain. Nat Neurosci 2010;13:133–140.
26. Dankort D, Curley DP, Cartlidge RA, Nelson B, Karnezis AN, Damsky WE Jr, et al. BRAF V600E cooperates with PTEN silencing to elicit metastatic melanoma. Nat Genet 2009;41:544–52.
27. Akinleye A, Furqan M, Mukhi N, Ravella P, Liu D. MEK and the inhibitors: from bench to bedside. J Hematol Oncol 2013;6:27.
28. Chan KT, Jones SW, Brighton HE, Bo T, Cochran SD, Sharpless NE, et al. Intravital imaging of a spheroid-based orthotopic model of melanoma in the mouse ear skin. Intravital 2013;2:e25805.
29. Stuhlmiller TJ, Miller SM, Zawistowski JS, Nakamura K, Beltran AS, Duncan JS, et al. Inhibition of lapatinib-induced kinome reprogramming in ERBB2-positive breast cancer by targeting BET family bromodomains. Cell Rep 2015;11:390–404.
30. Wang K, Singh D, Zeng Z, Coleman SJ, Huang Y, Savich GL, et al. MapSplice: accurate mapping of RNA-seq reads for splice junction discovery. Nucleic Acids Res 2010;38:e178–e178.
31. Li B, Dewey CN. RSEM: accurate transcript quantification from RNA-Seq data with or without a reference genome. BMC Bioinformatics 2011;12:323.
32. Love MI, Huber W, Anders S. Moderated estimation of fold change and dispersion for RNA-seq data with DESeq2. Genome Biol 2014;15:550.
33. Chen EY, Tan CM, Kou Y, Duan Q, Wang Z, Meirelles GV, et al. Enrichr: interactive and collaborative HTML5 gene list enrichment analysis tool. BMC Bioinform 2013;14:128.
34. Kuleshov MV, Jones MR, Rouillard AD, Fernandez NF, Duan Q, Wang Z, et al. Enrichr: a comprehensive gene set enrichment analysis web server 2016 update. Nucleic Acids Res 2016;44:W90–W97.
35. Gatza ML, Silva GO, Parker JS, Fan C, Perou CM. An integrated genomics approach identifies drivers of proliferation in luminal-subtype human breast cancer. Nat Genet 2014;46:1051–1059.
36. Fan C, Prat A, Parker JS, Liu Y, Carey LA, Troester MA, et al. Building prognostic models for breast cancer patients using clinical variables and hundreds of gene expression signatures. BMC Med Genomics 2011;4:3.
37. Jeck WR, Parker J, Carson CC, Shields JM, Sambade MJ, Peters EC, et al. Targeted next generation sequencing identifies clinically actionable mutations in patients with melanoma. Pigment Cell Melanoma Res 2014;27: 653–663.
38. Kakavand H, Rawson RV, Pupo GM, Yang JYH, Menzies AM, Carlino MS, et al. PD-L1 Expression and immune escape in melanoma resistance to MAPK inhibitors. Clin. Cancer Res 2017;23:6054–61.
39. Das Thakur M, Pryer NK, Singh M. Mouse tumour models to guide drug development and identify resistance mechanisms. J Pathol 2014;232: 103–11.
40. Cichorek M, Wachulska M, Stasiewicz A, Tymin´ska A. Skin melanocytes: biology and development. Adv Dermatology Allergol 2013;30:30–41.
41. Li JL, Goh CC, Keeble JL, Qin JS, Roediger B, Jain R, et al. Intravital multiphoton imaging of immune responses in the mouse ear skin. Nat Protoc 2012;7:221–34.
42. Rothstein EC, Nauman M, Chesnick S, Balaban RS. Multi-photon excitation microscopy in intact animals. J Microsc 2006;222:58–64.
43. Hanahan D, Weinberg RA. Hallmarks of cancer: the next generation. Cell 2017;144:646–74.
44. Long GV, Stroyakovskiy D, Gogas H, Levchenko E, de Braud F, Larkin J, et al. Combined BRAF and MEK inhibition versus BRAF inhibition alone in melanoma. N Engl J Med 2014;371:1877–1888.
45. Zawistowski JS, Bevill SM, Goulet DR, Stuhlmiller TJ, Beltran AS, Olivares-Quintero JF, et al. Enhancer remodeling during adaptive bypass to MEK inhibition is attenuated by pharmacologic targeting of the P-TEFb complex. Cancer Discov 2017;7:302 LP–321.
46. Tschandl P, Berghoff AS, Preusser M, Pammer J, Pehamberger H, Kittler H. Impact of oncogenic BRAF mutations and p16 expression on the growth rate of early melanomas and naevi *in vivo*. Br J Dermatol 2016;174: 364–370.
47. Nakasone ES, Askautrud HA, Kees T, Park JH, Plaks V, Ewald AJ, et al. Imaging tumor-stroma interactions during chemotherapy reveals contributions of the microenvironment to resistance. Cancer Cell 2012;21: 488–503.
48. Lu P, Weaver VM, Werb Z. The extracellular matrix: a dynamic niche in cancer progression. J Cell Biol 2012;196:395–406.
49. Shi H, Hugo W, Kong X, Hong A, Koya RC, Moriceau G, et al. Acquired resistance and clonal evolution in melanoma during BRAF inhibitor therapy. Cancer Discov 2014;4:80 LP–93.
50. Obenauf AC, Zou Y, Ji AL, Vanharanta S, Shu W, Shi H, et al. Therapy-induced tumour secretomes promote resistance and tumour progression. Nature 2015;520:368–372.
51. Hugo W, Shi H, Sun L, Piva M, Song C, Kong X, et al. Non-genomic and immune evolution of melanoma acquiring MAPKi resistance. Cell 2015;162:1271–1285.
52. Duncan JS, Whittle MC, Nakamura K, Abell AN, Midland AA, Zawistowski JS, et al. Dynamic reprogramming of the kinome in response to targeted MEK inhibition in triple-negative breast cancer. Cell 2012;149: 307–321.
53. Kim J, Lee Y, Cho HJ, Lee YE, An J, Cho GH, et al. NTRK1 fusion in glioblastoma multiforme. PLoS One 2014;9:e91940.
54. Weina K, Wu H, Knappe N, Orouji E, Novak D, Bernhardt M, et al. TGF-β induces SOX2 expression in a time-dependent manner in human melanoma cells. Pigment Cell Melanoma Res 2016;29:453–458.
55. Harris ML, Baxter LL, Loftus SK, Pavan WJ. Sox proteins in melanocyte development and melanoma. Pigment Cell Melanoma Res 2010;23: 496–513.
56. Cieply B, Farris J, Denvir J, Ford HL, Frisch SM. Epithelial–mesenchymal transition and tumor suppression are controlled by a reciprocal feedback loop between ZEB1 and Grainyhead-like-2. Cancer Res 2013;73:6299 LP–6309.
57. The Cancer Genome Atlas Network. Genomic classification of cutaneous melanoma. Cell 2015;161:1681–1696.